1

2 An examination of beta dose attenuation effects in coarse grains located in sliced samples

3 I.K.Bailiff

4 Department of Archaeology, Durham University, Dawson Building, Durham University, South

5 Road, Durham DH1 3LE, UK

6 e-mail: Ian.Bailiff@durham.ac.uk,

7

8

9

10 **Abstract**

11 Previous work has demonstrated the feasibility of performing spatially resolved luminescence

12 measurements with sliced solid materials (e.g., rock and ceramic) to determine the cumulative

13 absorbed dose to individual luminescent grains *in situ*. In the present study, aspects of the

14 dosimetry of individual grains that are truncated during slicing were examined using radiation

15 transport simulations employing simplified geometries. The results of the simulations were

16 applied to model the effect of grain truncation on the dosimetry of grains, in particular the beta

17 attenuation factor and the laboratory beta source dose rate for whole and partial volumes of

18 individual spherical grains. Where a material contains a wide range of coarse grain sizes there

19 is the potential for misinterpreting the size of the parent grain on the basis of an examination

20 of the shape and size of the truncated grain section exposed in the slice surface. If the original

21 grain size is underestimated, which is likely, the simulations predict an overestimation of both

22 the beta attenuation factor and the laboratory source beta dose rate, the maximum extent of

23 which depends on the range of grain sizes present in the material. The simulations also

24 indicate that by limiting the depth from the surface within which the average absorbed dose is

25 determined, approximating the effects of opacity of the mineral, the magnitude of these

26 deviations is reduced. However, a consequence of particular interest deriving from these

27 results is that, when evaluating the age equation, the changes in the two quantities

28 compensate, acting to moderate the overall effect on the calculated age for an individual grain,

29 depending on the geometry of the grain and the composition of the sample material.

30

31

32

1. Introduction

Developments in the instrumentation for luminescence dating measurements, based on modified luminescence readers (Duller, 2004), spatially resolved detectors (Greilich et al., 2002; 2005; Clark-Balzan and Schwenniger, 2012; Chauhan et al., 2014; Kook et al, 2015) and laser scanning systems (Bailiff and Mikhailik, 2003), have provided the capability to measure OSL from individual grains of quartz and feldspar, enabling the determination of the equivalent dose, D_e, with sufficiently bright individual grains. Previous work with solid materials such as rock and ceramic (Greilich et al., 2005; Bailiff, 2006) has demonstrated the feasibility of performing spatially resolved measurements with sliced samples to determine D_e that, in principle, allow estimates of age to be obtained for individual grains *in situ*. In this paper dosimetry issues that arise when performing D_e determinations with individual grains within cut slices are identified and investigated by performing radiation transport simulations using simplified geometries, with a particular interest in examining their potential effect on the calculation of the luminescence age

1.1. Dosimetry issues

For spherical grains that are optically transparent, free of radioactive sources, of 'coarse' grain size and set in a medium containing a uniform distribution of lithogenic radionuclides, the value of D_e determined by applying OSL techniques to individual grains extracted from a disaggregated sample medium that were fully reset is expected to decrease systematically with increasing grain size. The form of reduction is governed largely by the effects of beta attenuation. Adopting the convention commonly applied in dating (Aitken, 1985), the β component of the dose rate to a coarse grain (averaged over its volume) is calculated from the product of the point absorber infinite matrix dose rate (IMDR) and the beta attenuation coefficient, (1-ϕ). The latter is the complement of the absorbed dose fraction, ϕ, because of a superposition property which follows from Mayneord's reciprocal dose rate theorem (Fitzgerald et al, 1967), which can be further exploited to advantage in radiation transport modelling calculations. Within an infinite medium of homogeneous activity, the removal of activity within a sphere of lesser radius (e.g., a grain) contained in the medium leads to a reduction of the average dose rate within the sphere by an amount corresponding to the integral dose within a sphere of the same physical composition and activity as the medium external to the sphere. This relationship is well approximated providing charged particle equilibrium is obtained within both the sphere and the surrounding medium, a condition that is usually met for quartz and feldspar grains in a silicate matrix (Brennan, 2003).

In previous work Brennan (2003), updating the earlier work of Mejdahl (1979), obtained values of the attenuation coefficient for different sizes of spherical grains by calculating the absorbed

dose fraction, ϕ, using a scaled dose point kernel function (DPK), F(s). The concept of the DPK had been introduced (Loevinger, 1956) to calculate the distribution of absorbed dose (in water) within spherical volumes about a point source as part of radioimmunological studies of biological cells and applied to uniform media. The DPKs calculated by Berger (1973) advanced earlier work on point beta source dose distributions (Spencer, 1959; Cross, 1968) by employing Monte Carlo methods to simulate electron transport that accounts for multiple scattering and energy loss fluctuations. The beta dose distribution about a unit point source of a particular isotope is referred to as the beta dose point kernel (DPK; Prestwich et al. 1983), which is usually calculated as a scaled DPK where the radial distance is expressed as the fraction of the CSDA range (continuous-slowing-down approximation; ICRU,1984). Using the DPK, the variation in absorbed dose with distance, s, from a point source (energy E_0) in a homogeneous medium (density, ρ), D(s), is given by

$$D(s) = \frac{E_0\,F(s)}{4\tau\rho s^2},$$ (1)

where the scaled DPK is required to meet the condition

$$\int_0^\infty F(s)ds = 1$$ (2)

Brennan calculated the DPKs for point sources in quartz for the three lithogenic source beta spectra using a Monte Carlo transport code (ITS ACCEPTP) and evaluated the (average) fractional absorbed dose, $\phi(r)$, within a sphere of radius r (representing a grain) by integrating Eqn 1 over the spherical volume, obtaining the expression

$$\phi(r) = \int_0^{2r}\left[1 - \frac{3}{4}\frac{s}{r} + \frac{1}{16}\left(\frac{s}{r}\right)^2\right]F(s)ds,$$ (3)

which is equivalent to that derived by Berger (1973), and where $\phi(r)$ is expressed as a fraction of the total energy released by the source (i.e., the IMDR). Integration of Eqn 1 over a spherical segment, which does not appear to have been reported previously, results in an expression for the integrand that is considerably more complex than Eqn 3, requiring three stages of integration and containing quartic terms in s. Its full evaluation is underway and will be reported elsewhere as it is beyond the scope of this paper (Bailiff and Slim, forthcoming), although some preliminary results are referred to in the discussion below.

A significant advantage obtained by using radiation transport simulation codes is the calculation of absorbed dose for any shape and size of volumes, providing their geometry can

1   be specified (Nathan, 2010; Guérin et al, 2012). In the simulations discussed below, the
2   sources are uniformly distributed within a volume that is also defined as the detector volume,
3   within which an average absorbed dose is calculated. For the purposes of the calculations
4   explored in this paper, a simple spherical geometry has been used to represent a quartz grain,
5   which is located within a solid sample medium (e.g., a ceramic or encapsulated sediment).

6

7   Where an experimental determination of D_e is performed with slices of a sample containing
8   transparent coarse grains truncated by the cutting process, the form of reduction in D_e with
9   grain size is (theoretically) expected to the same as for the parent grains providing the grains
10   are bisected (Bailiff, 2006). However, for a material containing spherical grains of equal radius
11   (monodispersed), a distribution of grain radii will be observed in the surface the slice, reflecting
12   differences in the degree of truncation of the grains. The distribution will be further extended
13   where a range of grain sizes (polydispersed) is present in the material. If the sample matrix is
14   opaque, an examination of the grain radius in the slice surface, R_s, may give rise to a potential
15   ambiguity in the estimation of the original (parent) grain radius, and hence increased
16   uncertainty in the value of the attenuation factor appropriate to the parent grain when it was
17   located in the intact sample matrix. As the distribution of absorbed dose within the interior of
18   a single luminescent grain due to α and β radiation from sources external to the grain is
19   spatially not uniform (and the distribution of recombination centres within a grain may also not
20   be uniform), the relative contributions to D_e are affected by grain truncation. In these
21   circumstances uncertainty in the assessment of the parent grain size has implications for the
22   calculation of the beta attenuation factor $(1-\phi)$.

23

24   A second issue related to truncation that requires examination is the dose rate delivered by a
25   laboratory beta source to a truncated grain exposed in the surface of a slice, where the source
26   dose rate has been calibrated using whole grains. In addition to the (known) variation in the
27   dose rate with radial distance from the central axis of the source, the dose rate to the grain can
28   be expected to vary with the spatial extent of the grain below the cut surface.

29

30   Both issues are further influenced by the opacity of the mineral from which the grain is formed,
31   affecting the volume within which the absorbed dose is determined using OSL techniques.

32

33   **2. Dosimetry Models**

34   Two dosimetry models, A and B, were constructed for use with the general-purpose
35   radiation transport code MCNP (Goorley et al., 2013). The physical geometry of a model coded
36   for use with MCNP forms a central role in defining the simulation environment, as outlined in
37   the following sections for models A and B (further details in the Supplementary Material Sec.

SM1). The simulations provided a calculated precision of 1-2% in most cases (after 10^6-10^{10} particle histories), and this level of uncertainty does not reflect the larger uncertainties that would be encountered with experimentally determined quantities. Although diameter is commonly used in physical descriptions of granular materials, the radius is specified in the MCNP code, and is retained in the following discussion.

2.1 Model A geometry: β attenuation factor

The model was configured to examine the calculation of ϕ for an individual spherical quartz grain, located at the centre of an inert ceramic matrix containing a uniform distribution of sources of one of the lithogenic radionuclides (U, Th or K). Truncation of a grain arising from the cutting process was represented by the intersection of a sphere and the cutting plane, creating two volumetric sections defined as the detector volumes, where the smaller and larger volumes are referred to as the cap and base respectively (Fig. 1). For a sphere of radius R_{WG}, the volume is divided into two parts at height, h, and for the purposes of modelling, the division is without loss of volume, where the surface radius, R_S, of both cap and base are the same (which is not a necessary physical requirement in applying the results of the simulations). If a second cut is made to produce a slice of thickness T, and the size of the sphere is sufficient to cause h to exceed T, a large sphere will be truncated twice and, in this case, the base volume is further divided, having a radius in the lower surface of R_b. Additional variations were also included in the model geometry, comprising layers of 100 μm and 300 μm thickness below and parallel to the upper cut surface (L1, 100 μm and L3, 300 μm; not shown in Fig. 1 but included in Fig. SM2, Supplementary Material) within the base section to approximate the effect of grain opacity. The model A geometry was constructed with a sample slice thickness of 1 mm and with the parent grain radius (R_{WG}), ranging from 60 to 2000 μm. The simulations calculate the energy deposited in each of the two detector volumes. To relate the simplified geometry of the model to the physical application, the spherical detector volume is referred to in the following discussion as a (spherical) grain.

2.2 Model B geometry: Laboratory β source dose rate

The calculation of the beta dose rate delivered by a ^{90}Sr/^{90}Y laboratory source to quartz detector volumes located within and below the cut surface of a 1 mm-thick ceramic slice was simulated using model B. The simulations employed several geometric forms of quartz detector volumes, including a) discs and b) whole and truncated spheres presenting a specified radius at the cut surface, but having differing values of parent grain radius before cutting, ranging from 60 to 2000 μm (examples of several grain cross-sections are given in the Supplementary Material, Fig. SM2). The simulations take into account a contribution to dose

1
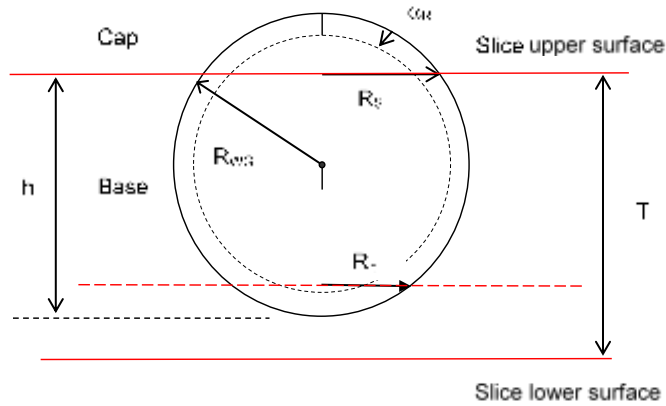
2
3 **Figure 1**
4 Details of spherical geometry of parent grain, radius R_{WG}, used in the MCNP simulations showing the
5 cross-section of a spherical grain and the positions of the upper and lower surfaces of a slice of
6 thickness T (in this case $T<2 \cdot R_{WG}$) caused by cutting. The surface radii of the doubly truncated
7 (hypothetical) grain in the upper and lower surfaces are given by R_S and R_b respectively. For the
8 purposes of the simulation, the two grain volumes produced by the cutting process are referred to as
9 the cap and base sections, as indicated. The inner circle (dotted line) indicates the outer volume of
10 the grain penetrated by alpha particles to an average depth α_R and is relevant to the assessment of
11 the total dose rate to a whole grain.
12

13
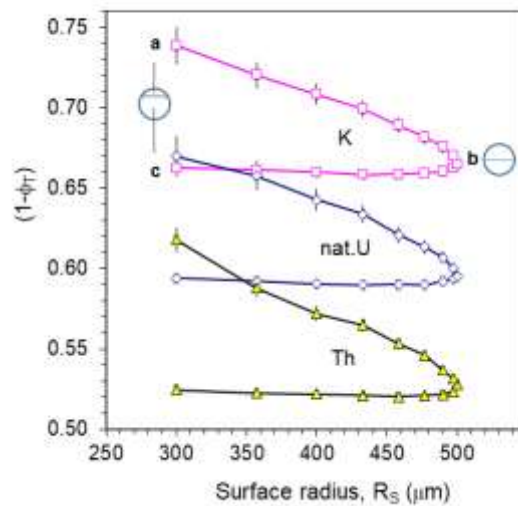
14 **Figure 2**
15 Variation in the attenuation factor, $(1-\phi_T)$, for β radiation with extent of truncation for a quartz grain
16 (ρ=2.65 g cm^{-3}) of 500 μm radius set in a ceramic medium (average density 1.8 g cm^{-3}) containing a
17 uniform distribution of sources (^{40}K, ^{238}U/^{235}U and ^{232}Th). The points a, b and c indicate, in the case of
18 the ^{40}K data, key stages in the change in grain volume with truncation height, h, translated to R_S (see
19 Fig. SM1, Supplementary Material), where point b represents a bisected grain; in moving from **a** to **b**
20 the cap volume increases and in moving from **c** to **b** the base volume increases. The lines are drawn
21 to indicate trends in data values and are not represent functions fitted to the data.

6

within the slice from backscattered radiation generated at the interface with a stainless steel sample mounting plate.

The detector volumes in the simulations comprised:

i) A continuous stack of quartz discs (1 mm rad. and thicknesses of 25 μm to a depth of 200 μm, and 50 μm thickness thereafter) extending from the surface to the base of a 1 mm-thick slice;

ii) Truncated spherical quartz grains of various parent grain sizes (R_{WG}, 500 to 1700 μm) presenting a surface radius (R_s) of 500 μm. The model was also configured with layers, parallel to the cut surface, of increasing depth (100-600 μm) within the truncated grain to represent the effects of grain opacity (examples in Fig SM2, Supplementary Material).

The simulations were performed for detector volumes located on the central vertical axis and along a parallel axis offset by 5 mm to examine for radial dependence. The source dose rate to each detector volume was calculated using an expression similar to Eqn 4 (below), where the value of the source activity used was 7.5 10^8 Bq.

A simplified irradiation geometry was employed comprising the ceramic slice mounted on a stainless steel base plate (thickness 0.5 mm) that rests on a 0.5 mm-thick nickel-chromium heater plate. The geometry was constructed with two source-to-sample separation distances, representing the configurations of a typical Risø reader irradiator (6.5 mm; also including a 125 μm-thick beryllium screen interposed between the sample and source) and a manually operated irradiator (14 mm) constructed in this laboratory (Bailiff, 1980).

2.3 Source terms

Model A. The simulations were performed separately for each of the three lithogenic sources distributed in the ceramic medium surrounding the grain. These included ^{40}K and the ^{238}U/^{235}U and ^{232}Th decay series (referred to as K, nat. U and Th sources, where the abundance of ^{235}U in natural uranium was taken to be 0.72%). The uranium and thorium progeny were assumed to be in secular equilibrium, although the simulations can be performed with any selected chain members. Details of the sources of the energy spectra for the lithogenic radionuclides are given in the Supplementary Material (Sec. SM1.2)

Model B. The source in model B was based on a reported (Aitken, 1985; p118) construction of the Amersham type SIPQ source installed in our irradiators, where the ^{90}Sr/^{90}Y sources were uniformly deposited on a silver disc (6 mm rad. x 20 μm) and covered by an additional 100 μm-

1   thick layer of electrodeposited silver. The primary β particle energy spectrum was obtained

2   from the MIRD database.

3

4   *2.4 Calculation of dose rate*

5   The statistical parameter in MCNP that forms the basis of absorbed dose calculations is the

6   *F8 tally (Forster et al., 2004), the average energy deposited (MeV) in the detector volume(s)

7   specified in the model. The average dose rate within the detector volume was calculated using

8   the dose rate coefficient $\dot{D_c}$ (mGy a^{-1}),

9 $$\dot{D_c} = \frac{E(\,^*F8)}{m_D} \times C \times P_D \times A_P \times m_S \,,$$ (4)

10   where m_D is the mass of the detector (g), C is a lumped scaling factor (5.0558) for energy and

11   time units, P_D is the probability of decay per unit parent disintegration, A_P is the specific activity

12   of the parent (Bq g^{-1}) and m_S is the mass of the source (g).

13

14   The beta absorbed dose fraction, ϕ, was calculated using the values of $\dot{D_c}$ and the beta IMDR

15   calculated on the basis of full energy release using the same energy spectra data as employed

16   in the simulations (for K, nat. U and Th, assuming uniformly distributed sources. The subscript

17   T is applied to denote where the detector volume is a spherical segment.

18

19   **3. Simulation results**

20

21   *3.1 Model A: beta attenuation factor*

22   The dose rate coefficients produced by each run of simulations of model A were used to

23   calculate the values of, ϕ_T , for both base and cap sections of a truncated grain where,

24        $\phi_T = \dot{D}_C^T // \dot{D}_C^{WG}$ (5)

25   and where $\dot{D}_C^T$ and $\dot{D}_C^{WG}$ are the dose rates for the cap or base sections and the parent grain,

26   respectively, calculated using Eqn 4.

27

28   The change in the value of the attenuation factor, $(1-\phi_T)$, with extent of truncation (h), translated

29   to surface radius, R_S, is illustrated in Fig. 2 for a grain of radius 500 μm (R_{WG}) and for the three

30   sources (K, nat. U and Th). At point *a* (Fig. 2, K) the corresponding value of h is small (100

31   μm; see Supplementary Material Fig. SM1 for conversion of h to R_S), associated with a cap

32   section, and the value of $(1-\phi_T)$ is higher than that for a whole grain due to the predominance

33   of the outer volume of the grain within the cap section. At point *b*, where the grain is bisected,

34   the value of $(1-\phi_T)$ is equivalent to that for a whole grain and thereafter, as the volume of the

35   base section progressively increases (to point *c*), the change in the calculated value of the

attenuation factor is only slight. Preliminary evaluation of Eqn 1 for a spherical segment using the transport equation developed by Loevinger (1956) in the place of Berger's DPK, produced the form of variation in the relative attenuation coefficient similar to that shown in Fig. 2. In general terms, the variation observed reflects the effect of a volumetric weighting factor on the non-uniform distribution of dose within a sphere when integrating Eqn 1 over a spherical segment (further discussion in Supplementary Material, Section SM3).

For the range of values of truncation depth examined, the maximum relative difference in the values of $(1-\phi_T)$ for R_S=300 μm (*a* vs *c*) is 11%, 13% and 18% for K and nat. U and Th sources respectively. Simulations performed with larger grains of 1 and 2 mm radius (R_{WG}) show similar behaviour, but with larger relative differences in the attenuation factor for an equivalently scaled size of R_S (60% R_{WG}). The relative increases in the value of $(1-\phi_T)$ are 30%, 27% and 33% for a 1 mm radius grain and 75%, 62% and 61% for a 2 mm radius grain (given in the order of K, nat. U and Th sources). The increases are broadly proportional to grain size for the nat. U and Th sources, but there is a greater divergence for the K source within this size range, reflecting its lower energy β spectrum. Hence, providing at least half the grain remains within the slice (between points *b* and *c* in Fig. 2), these simulations indicate that the resulting error would be small for monodispersed (single radius) truncated detector grains if the attenuation factor were calculated assuming a bisected grain.

In a sample medium containing a population of polydispersed detector grains (i.e., with different values of radius), however, truncation gives rise to an observed value of R_S that may correspond to parent grains of differing sizes truncated at various heights, h. Using the data from the model A simulations, the beta attenuation factors were calculated for truncated grains that presented three sizes of surface radius (R_S = 250, 500 and 1000 μm), and expressed as a fraction of the beta attenuation factor for the parent grain of the same radius (i.e., R_{WG}=R_S). The values obtained are plotted in Figs. 3a-c for K, nat. U and Th sources for one of the above values of surface radius (R_S=500 μm). The form of the changes in the relative attenuation factor with R_{WG}, as plotted, is broadly similar for the three source types, although the values of attenuation factor differ, reflecting differences in their β particle energy spectra. As in Fig. 2, the point of inflexion ($(1-\phi_T)/(1-\phi_{WG})$ =1) corresponds to a bisected grain (R_S=R_{WG}) and the data obtained for the cap and base sections are indicated by shaded symbols linked by broken and solid lines respectively. The bars linked by a broken line represent the values of relative attenuation factors calculated for layers L1-L3 in the base section; these have progressively lower values with increasing depth, as shown for L1 (100 μm) and L3 (300 μm). The values of

9
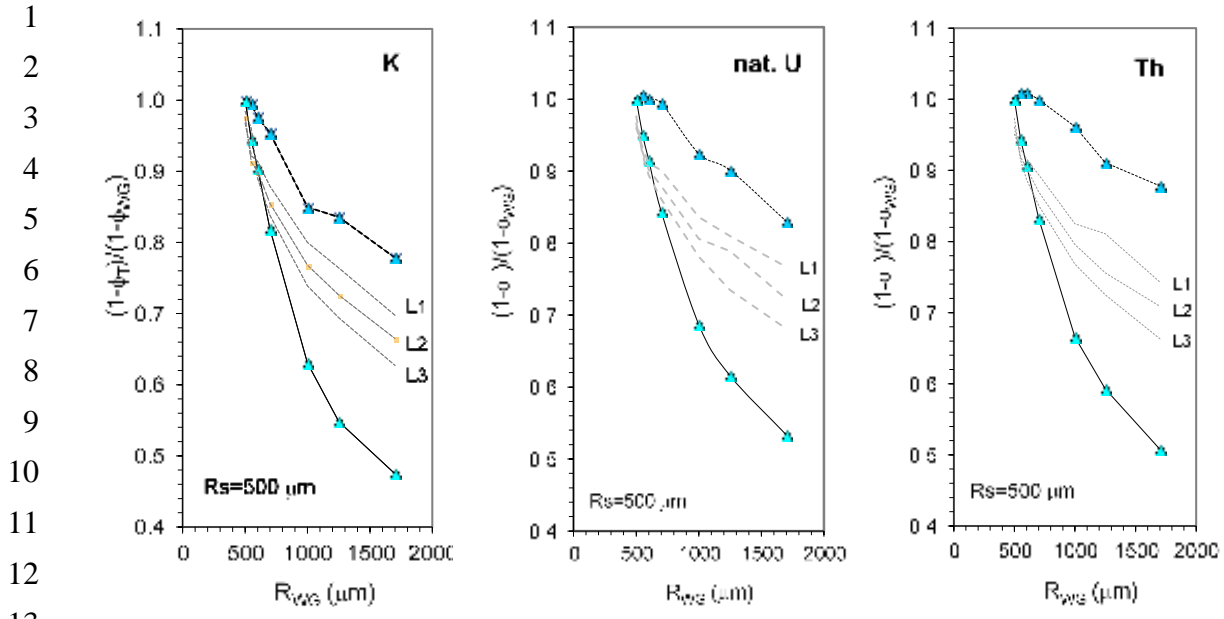
Figure 3
Values of the beta attenuation factor $(1-\phi_T)$ relative to that for a whole grain $(1-\phi_{WG})$ vs whole grain radius, R_{WG}, for spherical grains presenting a truncated surface radius of $R_S = 500$ μm, calculated using model A. These characteristics are shown for a) K sources, b) nat. U sources and c) Th sources. The values obtained for the cap and base sections are indicated by broken and solid lines respectively that link the data points; the point of inflexion corresponds to a bisected grain, where $(1-\phi_T)/(1-\phi_{WG})=1$. The bar symbols linked by a broken line indicate the values calculated for three layers lying below the cut surface of the grain, L1-L3, each of increasing thickness from 100 to 300 μm, defined as a proxy for grain opacity, as discussed in the main text. The lines are drawn to indicate trends in data values and do not represent functions fitted to the data.
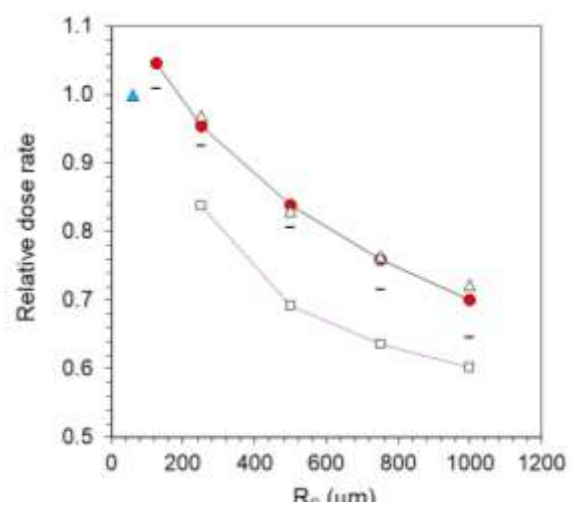
Figure 4
Dose-rate (β) to quartz grains of various values of surface radius R_S in a ceramic slice of 1 mm thickness calculated using Eqn 2, as discussed in the main text. The radionuclide composition of the matrix is typical (Th, 40 Bq kg^{-1}; nat. U, 40 Bq kg^{-1} U; K, 300 Bq kg^{-1}) and the quartz grains are free of sources; the alpha efficiency is 6%. The symbols indicate differing geometries and treatment of quartz grains: filled circles (bisected truncated grains in slice); filled triangle, HF etched; open squares and open triangles represent, respectively, base and cap sections of truncated grains in the slice where the parent grain radius is 2×R_S; bar (300 μm deep layer from cut surface of truncated grain). The lines are drawn to indicate trends in data values and do not represent functions fitted to the data.

10

1   the relative attenuation factor for other values of R_S (250 and 1000 μm) exhibit broadly similar

2   behaviour (not shown due to space limitations).

3   The influence of these potential variations in the beta attenuation factor on the calculation of

4   the dose rate to an individual grain in a slice is illustrated in Fig. 4 for quartz grains, free of

5   radioactivity, in a slice cut from a homogeneous (dry) sample matrix of typical radionuclide

6   composition (Th, 40 Bq kg^{-1}; nat. U, 40 Bq kg^{-1}; K, 300 Bq kg^{-1}). The total dose rate, $\dot{D}_{SGn}^{tot}$, was

7   calculated using a formulation based on that described previously (Bailiff, 2006;

8   Supplementary Material, Sec. SM2), taking into account external α, β, γ and cosmic radiation,

9   for the following detector volumes of individual quartz grains a) bisected grain b) cap and base

10   sections of grains presenting a surface radius, R_S, where R_{WG} was set to 2R_S, c) layer L3 of

11   300 μm depth within the base section of the grains described in b). All the values of dose rate

12   were normalised to the dose rate to a 60 μm radius HF etched quartz grain (filled triangle). The

13   linked data points for bisected grains (filled circles; R_{WG} = 125, 250, 500, 750 and 1000 μm)

14   trace the progressive reduction in dose rate with increasing parent grain size, reducing by

15   some 30% between 250 and 1000 μm radius. The dose rate to the cap (open triangles) and

16   base (open squares) sections of truncated grains (b) were calculated for four sizes of surface

17   radius (R_S= 250, 500, 750 and 1000 μm) for each size of the parent grain (R_{WG} = 2R_S).

18

19   For coarse grains with sizes extending to the millimetre range, free of internal sources and

20   dispersed in a uniform matrix, the values of cumulative dose are expected to lie on or below

21   the profile defined by the bisected grains. With an imposed restriction on the relative size of

22   the parent grain (R_{WG} = 2R_S), the dose rate to the truncated grains would be underestimated

23   by up to 15% (average) if the grains were assumed to have been bisected, but it would be

24   effectively unchanged for cap sections (+1% average). Although the dose rate to the cap

25   sections might be expected to be lower than that to the bisected grain ($R_{WG}=R_S$), its volume

26   contains the outer layers in the grain which receives a proportionately higher dose contribution

27   from external α and β radiation, giving rise to a dose rate similar to that for a bisected grain.

28   For layer L3 (300 μm) in the base section the alpha dose contribution to the dose-rate is

29   proportionately much less than for the cap section and, following a similar trend, the dose rate

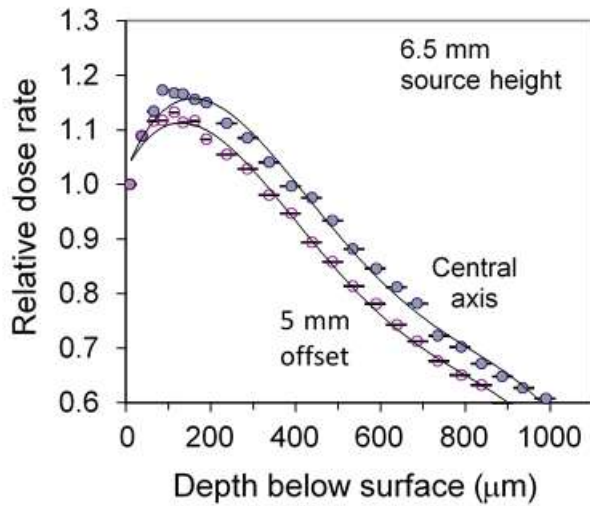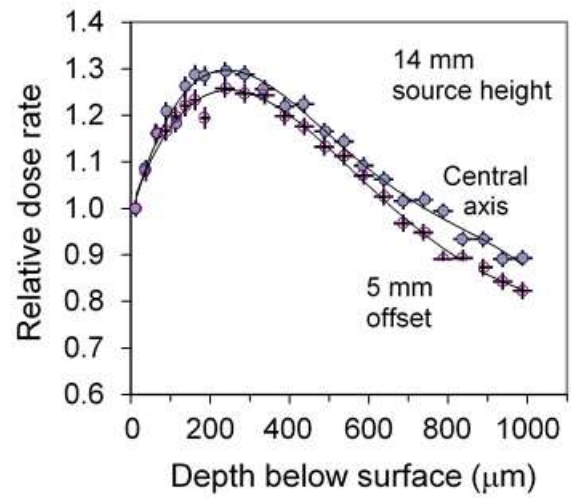30   values fall between those for the bisected and base sections of grains.
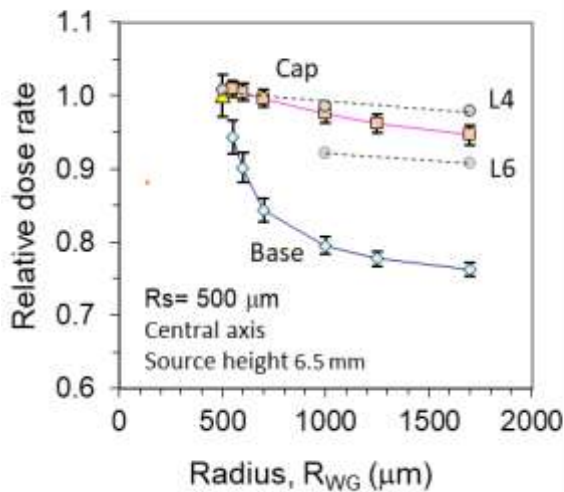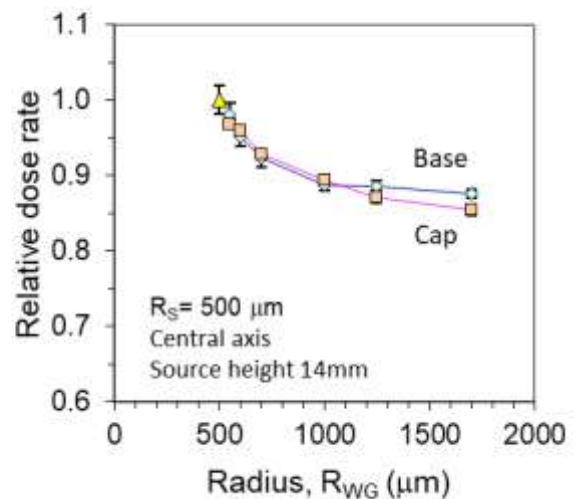
31

32

33

34

35

a)

b)

c)

d)

Figure 5

a,b) Depth-dose profiles of the β dose rate from the ^{90}Sr/^{90}Y beta source located at heights of 6.5 mm (a) and 14 mm (b) to quartz disc detector volumes in the 1 mm-thick ceramic slice, as discussed in the main text. The profiles have been calculated along the central axis of and at an offset radius of 5 mm; the dose rate values are normalised to the first sub-surface detector disc.

c,d) Variation of relative dose rate to the base and cap sections of truncated polydispersed spherical quartz grains of various parent grain sizes, R_{WG}, that present the same surface radius, R_S, of 500 μm, calculated using model B, where the source heights of c) 6.5 mm and d) 14 mm are indicated.

The lines are drawn to indicate trends in data values and do not represent functions fitted to the data.

12

3.2 Model B: Laboratory beta source dose rate

The calculated depth-dose rate profiles for the disc detectors of configuration (i) in a 1 mm-thick ceramic slice with the two source height geometries used in these simulations are shown in Fig. 5a (6.5 mm) and Fig 5b (14 mm) as relative values along the central axis and along the offset axis. The form of the profiles is governed by the depth of the build-up layer in the sub-surface of the slice, the progressive effects of attenuation and by backscattered radiation in the region of the interface with the steel substrate. The main differences in the profiles for the two source heights are: a) the extent of the build-up layer (ca 100 and 200 μm for 6.5 and 14 mm source heights respectively), b) the rate of reduction in dose rate is significantly greater for the lower source height (e.g., 60% vs 90%, respectively, at a depth of 1000 μm, relative to the sub-surface dose rate) and c) the radial dependence of dose rate, where a reduction of ca 35% vs 16% is predicted between the central axis and the 5 mm offset for the lower and higher source heights respectively. The profile along the central axis shown in Fig. 5b is qualitatively similar in form to the experimental profile obtained by Wintle and Murray (1977) using a dosimetry phosphor and aluminium absorbers, and also to a calculated profile reported by Greilich et al. (2008).

The results of the simulations performed using configuration (ii) of model B to examine the variation in dose rate to truncated spherical polydispersed spheres within the slice reflect the behaviour of the depth-dose profiles. Using the above example (Rs=500 μm; source height 6.5 mm), the simulations for a truncated grain (Fig. 5c) predict a modest reduction in the dose rate (relative to a bisected grain) with parent grain size for the cap sections, but a stronger reduction to the base sections, leading to a ~25% lower value for larger parent grains. For a source height of 14 mm, the changes in the dose rate to the cap and base sections with parent grain size are similar (Fig. 5d). However, the simulations indicate a complex change in the relationship between the cap and base section characteristics for the other two surface grain sizes (R_S=250 and 1000 μm; not shown) that switch within an overall span of ±10% about the value for a bisected grain, with the characteristics shown in Fig. 5d being at a cross-over point. The calculated dose rates to two layers (L4, 400 μm; L6, 600 μm, shown as bars in Fig. 5c), indicate a much-reduced effect for relatively large truncated grains.

4. Discussion

4.1 Beta attenuation factor

The use of the model A simulations to obtain values of ϕ indicate that for the simplest sample matrix with a monodisperse population of coarse grains, the effect of changing the surface

1   radius, R_S, of truncated grains is relatively benign for base sections providing more than half

2   the grain remains within the slice. As R_s progressively reduces, the value of the attenuation

3   factor for the cap increases, leading to an underestimation of the beta dose rate by 12-18%

4   (depending on the lithogenic source) if the cap sections were assumed to be base sections. In

5   the case of a polydisperse population of coarse grains, there is the potential for a greater

6   overestimation of the beta dose rate to either cap or base sections of a truncated grain,

7   depending on the full range of sizes of parent grains present in the sample matrix. The degree

8   of variation in the beta attenuation factor (Fig. 3) is significantly larger for the base section

9   compared with that for the cap section in the example shown (R_S=500 μm).

10

11 By applying OSL techniques to an individual grain to determine D_e, the volume from which the

12 luminescence is detected effectively corresponds to the volume within which the absorbed

13 dose is determined. Where a grain is transparent to UV wavelengths (i.e., the detection window

14 used for quartz OSL), the calculation of (1-ϕ_T) for the full base and cap section volumes is

15 appropriate. In the case of opaque grains, the values of (1-ϕ_T) calculated for layers in the base

16 section indicate the potential for reducing a potential underestimation of the external grain beta

17 component of the total dose rate, if the grains are (erroneously) assumed to be bisected (where

18 R_{WG}>R_S). In the absence of published data on the opacity of single grains, the measurements

19 by Aitken and Wintle (1977), although measured at wavelengths (~400 nm) higher than the

20 quartz OSL emission band, are of relevance: the flint with the highest opacity they examined

21 produced a value of 150 cm^{-1} for the optical attenuation coefficient, μ, which corresponds to a

22 reduction of 80% in optical transmission at a depth of 300 μm.

23

24 *4.2 Laboratory source dose rate*

25 For a slice containing a population of polydisperse grains, the dose rate (Fig. 5c,d) to a

26 truncated grain, $\dot{D}_{SGn}^{Sr}$, varies, for a given source height, in a complex manner according to grain

27 size and geometry. If a wide range of grain sizes is present in a sample the dose rate to the

28 base section may be substantially lower than that for bisected grains, although typical materials

29 are likely to have a smaller range than that explored in these simulations. With the more

30 commonly encountered source height of 6.5 mm, the dose rate to a truncated grain with a 500

31 μm surface radius where the parent grain was double this radius (R_{WG}=2R_S) is predicted to be

32 20% lower than for a bisected grain (located on the central axis). Again, if the 'optically active'

33 volume within the grain is limited (L4 and L6 in Fig. 5c), the differences in the dose rate relative

34 to a bisected (transparent) grain are predicted to be substantially reduced.   In these

35 circumstances the source dose rate may also be similar to that calculated for a cap section,

36 the volume of which is likely to be comparable. The characteristics predicted by the simulations

1   for a 14 mm source height indicate (consistent with expectation) smaller changes in dose rate

2   (Fig. 5d) with parent grain size. Using the same example (R_S= 500 μm; R_{WG}=2R_S), the dose

3   rate to the base section reduces by ~12% relative to a bisected grain, but the cap section also

4   shows a similar reduction, which differs to that calculated for the lower source height.

5

6   The simulations highlight further issues related to the calibration of the laboratory source.

7   Following the procedures applied with granular samples (e.g., Hansen et al., 2015), the

8   delivery of a known dose to a slice from a reference gamma source provides the opportunity

9   to calibrate the dose rate delivered by the laboratory source to individual grains exposed in a

10   slice surface using a spatially-resolved OSL measurement procedure. Where the minerals are

11   transparent, the dose rate to an individual grain is expected to reflect the size of the extant

12   grain. In practice, the dose rate is unlikely to be proportional to volume because of variations

13   in opacity between and within grains. Although, for opaque grains, the procedure would

14   account for the effects of an optically active depth that is less than the size of the grain, the

15   laboratory source dose rate evaluated is expected to approach that for a bisected grain (Fig.

16   5c). In these circumstances an assessment of the size of the parent grain made on the basis

17   of the grain-specific calibrated dose rate for the purposes of calculating the attenuation factor

18   is likely to be incorrect (e.g., in the case of L4 shown in Fig. 5c, an outer shell of the parent

19   grain is the dosimetry volume of interest).

20

21   *4.3 Effect on luminescence age calculation*

22   The above simulations indicate that if a truncated grain is incorrectly assumed to have been

23   bisected, the omission of the adjustment to the (total) dose rate due to lithogenic sources of

24   radiation, $\dot{D}_{SGn}^{tot}$, and the laboratory beta source dose rate, $\dot{D}_{SGn}^{Sr}$, fortunately act in a

25   compensating manner if both quantities require adjustment in the same direction (i.e., reduced

26   or increased) because of their reciprocal positions in the age equation. Continuing to use the

27   same example (R_S=500 μm; R_{WG}=2R_S), the beta attenuation coefficient, and in turn the total

28   dose rate, $\dot{D}_{SGn}^{tot}$ is predicted to be overestimated by ~20% (Fig. 4) if the truncated grain is

29   assumed to be bisected. Where the laboratory source height is ca 6.5 mm, and the same

30   assumption concerning parent grain size is made, the dose rate used in evaluating D_e would

31   also be overestimated, by ~20%. Consequently, when evaluating the quotient (Age =D_e/$\dot{D}_{SGn}^{tot}$),

32   the changes in values of the two quantities compensate and, for this example, the effect on

33   the luminescence age is predicted to be close to neutral. If the grains were opaque and the

34   optically active volume is defined by L3 (upper 300 μm-thick layer in the base section), for

35   example, similar compensation would also occur, but with much smaller overestimates of D_e

36   and $\dot{D}_{SGn}^{tot}$. At a greater source height (14 mm), the calculated overestimate of the dose rate

($\dot{D}_{SGn}^{Sr}$) is significantly lower (~10%), leading to a small overestimate in the age. The compensating effect will apply to other grain sizes for the reason discussed above, but as the value of $\dot{D}_{SGn}^{Sr}$ varies according to both grain size and radial offset, a spatially-resolved (i.e., grain specific) approach to the analysis needs to be taken when examining for the effects of truncation on the evaluation of the age equation.

5. Conclusions

This study has used radiation transport simulations with simple spherical geometries to examine the effect of the truncation of grains in sliced samples on the calculation of the beta attenuation factor and the laboratory beta source dose rate. The results have highlighted the potential effect on the values of these two variables where a material contains a wide range of coarse grain sizes and where the size of the parent grain is misinterpreted on the basis of an examination of the grain radius in the cut surface. In general, an underestimation of the parent grain size is likely to arise, resulting in an overestimation of both the beta attenuation coefficient and the laboratory beta source dose rate, the maximum extent of which depends on the range of grain sizes in the material. The simulations also indicate that by limiting the depth from the surface of the truncated grain within which the absorbed dose is determined, approximating the effects of opacity of the mineral, the magnitude of these deviations is reduced. However, a consequence of particular interest deriving from these results is that, when evaluating the age equation, the changes in the two quantities compensate, acting to moderate the overall effect on the calculated age for a particular grain, depending on the geometry of the grain and the composition of the surrounding sample material. While radiation transport modelling is computationally direct and powerful in terms of extension of this approach to modelling heterogeneous materials, establishing a link to the physical models underpinning the analytical approach employing dose point kernels is nonetheless important, as it may enable analytical functions to be derived that can be applied in dosimetry calculations without the need to resort to simulations. However, in the case of complex materials containing heterogeneous distributions of lithogenic sources (e.g., Guerin et al., 2015; Martin et al., 2015), more elaborate computational models are required to calculate the dose to individual coarse grains in cut slices of solid (or encapsulated) material, and these can provide valuable predictive tools to augment experimental measurements that ultimately aim to derive age estimates for individual grains.

References

Aitken, M.J., 1985. Thermoluminescence Dating. Academic Press, London.

Aitken, M.J., Wintle, A.G., 1977. Thermoluminescence dating of calcite and burnt flint: the age relation for slices. Archaeometry 19, 100-105.

Bailiff, I.K., 1980. A beta irradiator for use at the Durham TL dating laboratory. Nucl. Instrum. & Meth. 175, 224-226.

Bailiff, I.K., 2006. Development of single grain OSL dating of ceramic materials: spatially resolved measurement of absorbed dose. Radiat. Meas. 41, 744-749.

Bailiff, I.K., Mikhailik, V.B, 2003. Spatially resolved measurement of optically stimulated luminescence and time-resolved luminescence. Radiat. Meas. 37, 151-159.

Berger, M.J., 1973. Improved point kernels for electron and beta-ray dosimetry. NBSIR 73-107; National Bureau of Standards, Washington D.C.

Brennan, B.J., 2003. Beta doses to spherical grains. Radiat. Meas. 37, 299-303.

Chauhan, N., Adhyaru, P. Vaghela H., Singhvi, A.K., 2014. EMCCD based luminescence imaging system for spatially resolved geo-chronometric and radiation dosimetric applications. J Instrum. P11016.

Clark-Balzan, L., Schwenninger, J-L, 2012. First steps toward spatially resolved OSL dating with electron multiplying charge-coupled devices (EMCCDs): System design and image analysis. Radiat. Meas. 47, 797-802.

Cross, W.G., 1968. Variation of beta dose attenuation in di3erent media. Phys. Med. Biol. 13, 611–618.

Duller, G.A.T., 2004. Luminescence dating of Quaternary sediments: recent developments, J. Quat. Science 19, 183–192.

Fitzgerald, J. J., Brownell, G. L., Mahoney, F. J., 1967. Mathematical theory of radiation dosimetry. Gordon and Breach, New York.

Forster, R.A., Cox, L.J., Barrett, R.F., Booth, T.E., Breimeister, J.F., Brown, F.B., Bull, J.S., Geisler, G.C., Goorley, J.T., Mosteller, R.D., Post, S.E., Prael, R.E., Selcow, E.C., Sood, A., 2004. MCNP^{TM} version 5. Nucl. Instrum. and Methods B 213, 82-86.

Goorley, T., James, M., Booth, T., Brown, F., Bull, J., Cox, L.J., Durkee, J., Elson, J., Fensin, M., Forster, R.A., Hendricks, J., Hughes, H.G., Johns, R.B., Kiedrowski, R., Martz, Mashnik, S., McKinney, G., Pelowitz, D., Prael, R., Sweezy, J., Waters, L., Wilcox, T., Zukaitis, T., 2013. Initial MCNP6 release overview, MCNP6 version 1.0. LA-UR-11-05198. (http://laws.lanl.gov/vhosts/mcnp.lanl.gov/pdf_files/la-ur-13-22934.pdf)

Greilich, S., Glasmacher, U.A., Wagner, G.A., 2002. Spatially resolved detection of luminescence – a unique tool for archaeochronometry. Naturwissenschaften 89, 371-375.

Greilich, S., Glasmacher, U.A., Wagner, G.A., 2005. Optical dating of granitic stone surfaces. Archaeometry 47, 645-665.

Greilich, S., Bøtter-Jensen, L., Murray, A.S., 2008. Simulation of electron transport during beta irradiation. Radiat. Meas. 43, 748-751.

Guérin, G., Mercier, N., Nathan, R., Adamiec, G., Lefrais, Y., 2012. On the use of the infinite matrix assumption and associated concepts: a critical review. Radiat. Meas. 47, 778-785.

Guérin, G., Jain, M., Thomsen, K.J., Murray, A.S., 2015. Modelling dose rate to single grains of quartz in well-sorted sand samples: The dispersion arising from the presence of potassium feldspars and implications for single grain OSL dating. Quaternary Geochronology 27, 52-65.

ICRU, 1984. International Commission on Radiation Units and Measurements. ICRU Report 37, Stopping Powers for Electrons and Positrons. International Commission on Radiation Units and Measurements, Bethesda, USA.

Kook, M.H., Lapp, T., Murray, A., Thomsen, K.J., Jain, M 2015, A luminescence imaging system for the routine measurement of single-grain OSL dose distributions Radiation Measurements, 81, 171–177.

Loevinger, R. 1956. The Dosimetry of Beta Sources in Tissue. The Point-Source Function, Radiology 66, 55-62.

Martin, L., Mercier, N., Incerti, S., Lefrais, Y., Pecheyran, C., Guérin, G., Jarry, M., Bruxelles, L., Bon, F., Pallier, C., 2015. Dosimetric study of sediments at the beta dose rate scale: Characterization and modelization with the DosiVox software. Radiat. Meas. 81, 134-141.

Mejdahl, V., 1979. Thermoluminescence dating: dose attenuation in quartz grains. Archaeometry 21, 61–72.

Nathan, R.P., 2010. Numerical modelling of environmental dose rate and its application to trapped-charge dating. Unpublished DPhil thesis. University of Oxford.

Prestwich, W.Y., Nunes, J., Kwok, C.S., 1989. Beta dose point kernels for radionuclides of potential use in radioimmunotherapy. J. Nuclear Med. 30, 1036-1046.

Spencer, L. V., 1959. Energy Dissipation by Fast Electrons, National Bureau of Standards Monograph 1, National Bureau of Standards, Washington D.C.

Wintle, A.G., Murray, A.S., 1977. Absorbed dose from a beta source as shown by thermoluminescence dosimetry. Int. J. Appl. Radiat. & Isotopes 28, 625-627.